Journal Pre-proof

Single Fe atoms confined in two-dimensional MoS$_2$ for sulfite activation: A biomimetic approach towards efficient radical generation

Li-Zhi Huang (Conceptualization) (Methodology) (Writing - original draft) (Project administration) (Funding acquisition) (Investigation), Xiuli Wei (Validation) (Investigation), Enlai Gao (Formal analysis), Chunbo Zhang (Formal analysis), Xin-Ming Hu (Writing - review and editing), Yiqun Chen (Supervision) (Funding acquisition), Zizheng Liu (Supervision) (Funding acquisition), Nicolas Finck (Formal analysis), Johannes Lützenkirchen (Writing - review and editing), Dionysios D. Dionysiou (Writing - review and editing)

Please cite this article as: Huang L-Zhi, Wei X, Gao E, Zhang C, Hu X-Ming, Chen Y, Liu Z, Finck N, Lützenkirchen J, Dionysiou DD, Single Fe atoms confined in two-dimensional MoS$_2$ for sulfite activation: A biomimetic approach towards efficient radical generation, *Applied Catalysis B: Environmental* (2019), doi: https://doi.org/10.1016/j.apcatb.2019.118459

This is a PDF file of an article that has undergone enhancements after acceptance, such as the addition of a cover page and metadata, and formatting for readability, but it is not yet the definitive version of record. This version will undergo additional copyediting, typesetting and review before it is published in its final form, but we are providing this version to give early visibility of the article. Please note that, during the production process, errors may be discovered which could affect the content, and all legal disclaimers that apply to the journal pertain.

Single Fe atoms confined in two-dimensional MoS$_2$ for sulfite activation: a biomimetic approach towards efficient radical generation

Li-Zhi Huang[a], Xiuli Wei [a,b], Enlai Gao[a], Chunbo Zhang[a], Xin-Ming Hu[c], Yiqun Chen[a,*], Zizheng Liu[a,*], Nicolas Finck[d], Johannes Lützenkirchen[d], Dionysios D. Dionysiou[e]

[a]*School of Civil Engineering, Wuhan University, No. 8, East Lake South Road, Wuhan 430072, China*

[b]*College of Environmental Science and Engineering, Tongji University, Shanghai 200092, China*

[c]*Carbon Dioxide Activation Center, Interdisciplinary Nanoscience Center (iNANO) and Department of Chemistry, Aarhus University, Gustav Wieds Vej 14, DK-8000, Aarhus C, Denmark*

Institut für Nukleare Entsorgung (INE), Karlsruher Institut für Technologie (KIT), Hermann-von-Helmholtz-Platz 1, 76344 Eggenstein-Leopoldshafen, Germany

[e]*Environmental Engineering and Science Program, University of Cincinnati, Cincinnati, Ohio 45221-0012, United States*

*Corresponding authors: yq.chen@whu.edu.cn (Y. Chen); lzz2015@whu.edu.cn (Z. Liu)

1

Graphical abstract
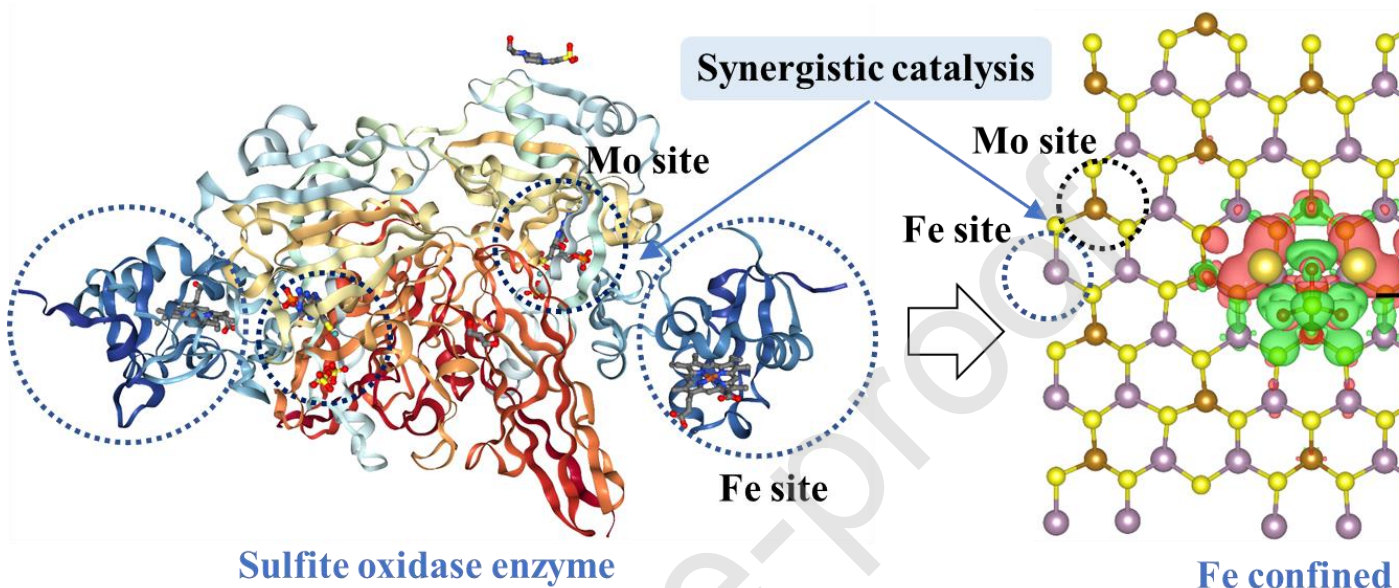
Highlights:

- Single Fe atoms confined in two-dimensional MoS_2 mimic sulfite oxidase enzyme.

- MoS_2 not only consists of Mo catalytic sites but also provides the support for Fe catalytic sites.

- Dual catalytic sites play collaboratively to obtain high reactivity for sulfite activation.

- 2D catalyst allows interpretation of catalytic performances using theoretical calculation.

Abstract

Sulfite has been recently recognized as a source of radicals for oxysulfur radical-based advanced oxidation process due to its low cost and low toxicity. Inspired by sulfite oxidase enzyme, we demonstrate single Fe atoms confined in two-dimensional MoS_2 nanosheets ($Fe_xMo_{1-x}S_2$) as highly reactive catalysts for heterogeneous activation of sulfite, thereby promoting efficient oxidative degradation of propranolol in water. Highest propranolol degradation efficiency of ~90% was observed at pH 4.0. The Fe or Mo sites of $Fe_xMo_{1-x}S_2$ activate sulfite *via* the Fe^{2+}/Fe^{3+} or $Mo^{4+}/Mo^{5+}/Mo^{6+}$ redox cycle. More importantly, the synergistic catalysis involving the Fe and Mo sites play an essential role. $SO_5^{\bullet-}$ is the major radical responsible for propranolol degradation with the 2nd-order rate constant of $(1.1\pm0.6)\times10^7$ M^{-1} s^{-1}. Furthermore, the $Fe_xMo_{1-x}S_2$/sulfite system is capable of degrading a wide range of recalcitrant organic pollutants and operating in a real water environment, suggesting its great potential in practical water treatment applications.

Keywords: sulfite activation; biomimetic; single atom catalyst; synergistic catalysis; advanced oxidation process.

1. Introduction

The oxidation of sulfite has been widely reported to generate reactive oxygen species (ROS) in both biotic [1] and abiotic [2] environment. Sulfite-derived ROS,

3

although detrimental to organisms, have been recently used in advanced oxidation processes for removal of contaminants [2]. Up to date, a variety of transition metal ion-based homogeneous catalysts [3], has been explored to oxidize/activate sulfite for ROS generation. These homogeneous catalysts usually possess superior activity and involve full exposure of the metal atoms for sulfite activation. However, homogeneous activation of sulfite in advanced oxidation processes causes heavy metal contamination in the treated water as well as other problems such as catalyst deactivation and sludge generation [2]. Heterogeneous catalysts, including Fe, Co, Cu, Ni, Mn-based nanomaterials, have been explored to solve these problems [2, 4]. These nanomaterials have advantages such as the negligible release of metal ions and excellent reusability after separating the catalyst from treated water [4]. However, these metal nanomaterials suffer from low utilizing efficiency of the metal atoms and low activity, as only atoms on the surface of metal nanomaterials are active for catalysis. Single-atom catalysts (SACs), with catalytically active single atoms anchoring to insoluble support, seems an ideal solution to combine the advantages of both heterogeneous and homogeneous catalysts in advanced oxidation processes [5], but this challenging approach has been rarely studied [6-8].

   In vivo, sulfite oxidation is catalyzed by an enzyme, sulfite oxidase. The high activity of sulfite oxidase originates from its atomically dispersed catalytic Fe and Mo sites which act cooperatively to promote the synergistic catalysis. An enzyme-catalyzed sulfite oxidation involves sulfite binding and oxidation on metal center, looping of Fe^{2+}/Fe^{3+} in the Fe center, looping of $Mo^{4+}/Mo^{5+}/Mo^{6+}$ in the Mo center, and several intramolecular reactions among Fe centers, Mo centers and cytochrome c (Figure S1) [9]. Fe and Mo

4

atoms coordinate with biomacromolecules to maintain single atomic isolation, and

protein loops connect Fe and Mo centers to allow their efficient interaction [10]. This

principle can serve as a guideline to discover synthetic inorganic materials for efficient

sulfite activation, but such a concept has not yet been studied.

MoS_2 has been intensively studied both as a catalyst itself and as a two-dimensional

(2D) support to confine SACs [11]. In light of the successful synthesis of 2D MoS_2

confining various single metal atoms, also known as metal doped MoS_2, (e.g. Pt, Co, Ni,

W, Zn, Mn and V) [12-15], we speculate that single Fe atoms confined in 2D MoS_2 may

mimic the synergistic Fe and Mo catalytic site in sulfite oxidase. In other words, they

possess dual catalytic sites which work collaboratively for efficient sulfite activation. The

confined Fe atoms in MoS_2 nanosheets may allow fast redox interaction between Fe and

Mo catalytic sites. Moreover, the single Fe atoms are stabilized and confined in the MoS_2

nanosheets, preventing the aggregation of Fe atoms into clusters or particles. While the

catalytic performance of Fe-based catalyst for sulfite activation is well-known [2], sulfite

activation by MoS_2 was recently realized by Fan et al. [16]. In their work, sulfite was

photoelectrochemically activated by a MoS_2 photoanode to generate oxysulfur radicals

for efficient conversion of ammonia to dinitrogen. Thus, it is speculated that sulfite may

be activated by the single Fe atoms confined in 2D MoS_2. Single metal atom doping in

MoS_2 support is usually obtained by bottom-up methods, such as

hydrothermal/solvothermal methods, chemical vapor transport/deposition, pyrolysis etc.

[11, 14, 17-19]. Among these routes, hydrothermal synthesis allows facile, low-cost and

potential up-scaled synthesis of single metal atoms doped MoS_2, which is promising for

practical environmental applications [20, 21].

5

Propranolol (PPA) was used as a target organic pollutant in this work, which is a beta-blocker widely detected in surface waters [22]. We demonstrate, for the first time, that MoS_2 nanosheets with confined single Fe atoms (designated as $Fe_xMo_{1-x}S_2$) exhibit outstanding activity for sulfite activation. The generated ROS, which efficiently degrades various persistent organic pollutants, were identified by electron spin resonance and radical scavenger experiments. The Fe content in $Fe_xMo_{1-x}S_2$ was modulated, allowing optimal adsorption energy to facilitate electron transfer for sulfite activation. The synthesized 2D MoS_2 structure not only consists of Mo catalytic sites but also provides the support for atomically isolated Fe catalytic sites. The experimental results and theoretical calculation suggest that these dual catalytic sites act collaboratively to obtain high reactivity for sulfite activation, mimicking sulfite oxidase enzyme (Figure 1). Our study details the first insights into the biomimetic approach to design a 2D MoS_2 confining single Fe atoms with synergistic catalytic sites for efficient degradation of organic pollutants.

2. Experimental

2.1 Chemicals and materials

All chemicals were supplied by Sinopharm Chemical Reagent Co., Ltd. The $Fe_xMo_{1-x}S_2$ catalysts were synthesized *via* a one-pot hydrothermal method [20, 23]. $FeSO_4 \cdot 7H_2O$, $Na_2MoO_4 \cdot 2H_2O$, and L-cysteine ($C_3H_7NO_2S$) were used as iron, molybdenum and sulfur source, respectively. A 200 mL aqueous solution consists of $Na_2MoO_4 \cdot 2H_2O$, $FeSO_4 \cdot 7H_2O$ and L-cysteine were used as a precursor for hydrothermal synthesis. The $Fe_xMo_{1-x}S_2$ catalysts with different x were synthesized by varying $Na_2MoO_4 \cdot 2H_2O/FeSO_4 \cdot 7H_2O$ ratios from 1/1, 1/3, 3/1, to 1/0 with the sum of molar

6

amounts at 12.5 mM. The concentration of L-cysteine was 66 mM for all the synthesis. The synthesis was carried out in a 300 mL autoclave at 200 °C for one day. The as-synthesized $Fe_xMo_{1-x}S_2$ catalyst was thoroughly washed with 1 M H_2SO_4, Milli-Q water and ethanol *via* filtration/re-suspension to remove any unreacted residual salts. Finally, the washed catalysts were dried in an oven at 65 °C and stored in a desiccated vessel until further use.

2.2 Catalytic degradation of pollutants

Degradation of 1-30 μM selected organic pollutants were carried out to evaluate the catalytic performance of the $Fe_xMo_{1-x}S_2$/sulfite system, using a catalyst dosage of 0.05-0.3 g/L. The sulfite or peroxide stock solution was always freshly prepared. The initial reaction pH was adjusted to 3-8 using 1 M NaOH or HCl solutions. The reaction was initiated by adding 0.1-2 mM sulfite or peroxide. Once the degradation was initiated, 2 mL samples were withdrawn from the reaction suspensions at given time intervals, immediately quenched by 50 μL ethanol, filtered by 0.22 μm filter paper and analyzed by a high-performance liquid chromatography (HPLC, Agilent). For the reuse of the catalyst, the catalysts were collected by filtration at the end of each experiment, washed with water and ethanol for 2-3 times, vacuum dried, and then used for the next cycle.

2.3 Analytical methods

The concentration of PPA, estriol, atenolol, benzoic acid, fluoxetine were quantified using HPLC equipped with a C18 column. The analytical conditions including mobile phase composition, wavelength, and retention time are shown in Table S1. Orange II, indigo and methylene blue were analyzed using a spectrophotometer at wavelengths of 485 nm, 610 nm, and 665 nm, respectively. The concentration of sulfite was quantified

7

using ion chromatography (Metrohm, 820). The degradation products of PPA were determined by liquid chromatography-mass spectrometry (LC-MS). X-ray photoelectron spectra (XPS) were obtained using a Kratos Axis Ultra^{DLD} instrument. All binding energies were calibrated to adventitious C (284.8 eV). High-resolution transmission electron microscopy (HRTEM) and high-angle annular dark-field scanning transmission electron microscopy (HAADF-STEM) images were obtained using an image spherical aberration-corrected TEM system (FEI Titan 60-300) with an accelerating voltage of 300 kV. Scanning electron microcopy (SEM) images were recorded by a Quanta 200 microscope (FEI Company, USA) operating at 10 kV. X-ray diffraction (XRD) data was obtained *via* a Malvern Panalytical X-ray diffractometer (XPert Pro). Electrochemical measurements of cyclic voltammetry and Tafel scans were carried out using a CHI 760C potentiostat (CH Instrument, USA). An undivided three-electrode cell was used with a Pt counter electrode and an Ag/AgCl (3.5 M) reference electrode. A glassy carbon electrode (diameter = 4 mm) was loaded with a given $Fe_xMo_{1-x}S_2$ catalyst and used as the working electrode. A volume of 10 mL 0.5 M Na_2SO_4 aqueous solution in the presence or absence of 0.1 M sulfite was used as supporting electrolyte.

2.4 Density functional theory calculation

In this work, density functional theory (DFT) calculations were performed using the Vienna *Ab*-initio simulation package (VASP) [24, 25]. The ion-electron interactions were described by the projector augmented wave potential [26]. General gradient approximation is used as the exchange and correlation functional parameterized by Perdew Burke, and Ernzerhof [27]. Plane-wave basis sets with an energy cutoff of 520 eV and *k*-point densities > 20 Å in reciprocal space were used in all calculations [28]. For

8

structural relaxation, the force on each atom is converged below 0.01 eV Å^{-1}. To avoid

periodic image interaction, a vacuum separation of 30 Å was used to isolate the system.

For the absorption calculation, the supercells with an in-plane size of 22.1 Å×22.3 Å and

a k-point mesh of 1×1×1 were used. Additional calculations with van der Walls

corrections of DFT-D3 method with Becke-Jonson damping [29] were performed to

validate the current approach.

3. Results and discussion

3.1 Synthesis and characterization of Fe$_x$Mo$_{1-x}$S$_2$

Fe$_x$Mo$_{1-x}$S$_2$ catalysts, where x = 0, 0.22, 0.36 and 0.51, were synthesized *via* a one-pot

hydrothermal method using FeSO$_4$, Na$_2$MoO$_4$ and L-cysteine as Fe, Mo and S sources,

respectively. The thermal decomposition of L-cysteine releases H$_2$S which reduces

MoO$_4^{2-}$ to MoS$_2$ [23]. The collision between Fe^{2+} and the free sulfur ends of MoS$_2$ may

allow incorporation of Fe atoms into 2D MoS$_2$ nanosheets [20]. Importantly, the atomic

ratio of Fe to Mo can easily be tuned by changing the ratio of Fe and Mo precursors

during hydrothermal synthesis. This bottom-up method has been reported as an effective

strategy to substitute Mo atoms with transition metal atoms (e.g. Ni, Fe, Co, Zn, and Mn)

in MoS$_2$ [11].

Fe$_x$Mo$_{1-x}$S$_2$ was thoroughly characterized to understand its structure. The chemical

composition of Fe$_x$Mo$_{1-x}$S$_2$ with various x was determined (MoS$_2$, Fe$_{0.22}$Mo$_{0.78}$S$_2$,

Fe$_{0.36}$Mo$_{0.64}$S$_2$ and Fe$_{0.51}$Mo$_{0.49}$S$_2$) by XPS, and the corresponding XPS survey spectra are

shown in Figure 2a. The binding energy of the Fe2p 3/2 peak for Fe$_x$Mo$_{1-x}$S$_2$ is 707.4 eV

(Figure 2b). As any possible occurrence of Fe metal in Fe$_x$Mo$_{1-x}$S$_2$ was removed by acid

washing, the observed binding energy indicates the confined Fe in MoS$_2$ support may

9

have a formal oxidation state of +2. For the Mo 3d XPS spectra, the major peak at 228.5

eV assigned to Mo^{IV} $3d_{5/2}$ confirms the dominance of Mo^{IV} in $Fe_xMo_{1-x}S_2$ catalyst (Figure

2c). The tiny peak at 235.5 eV can be assigned to Mo^{VI} $3d_{3/2}$ (Figure 2c), which may be

attributed to the oxidation of Mo^{IV} by oxygen at ambient conditions. The S 2s orbital

results in a small peak at 226.0 eV. A doublet ($S2p_{1/2}$, 162.9 eV; $S2p_{3/2}$, 161.8 eV) shown

in S 2p high resolution XPS spectra confirms the −2 oxidation state of sulfur in $Fe_xMo_{1-x}S_2$ (Figure 2d) [20]. It should be noted that a positive shift (~0.2 eV) in the Mo 3d XPS

spectra was observed upon Fe doping. Also, the S 2p XPS spectra in the $Fe_{0.36}Mo_{0.64}S_2$

shift positively by ~0.4 eV relative to those in the pristine MoS_2. These shifts were

further investigated by theoretical calculations on the charge transfer among Fe, Mo, and

S atoms in $Fe_xMo_{1-x}S_2$ catalyst. The changed charge transfer of Mo and S in MoS_2 after

Fe doping confirms an increased formal oxidation state of Mo and S (Figure S2), which is

in line with the positive shift of Mo 3d and S 2p XPS spectra (Figure 2c-d). These shifts

demonstrate the perturbation of the electronic structure of MoS_2 upon Fe doping, which

may trigger the redox activity as well as the catalytic performance of MoS_2 [11].

The (002) diffraction peak of MoS_2 (PDF#73-1508) at 14.4° is not observed in the

$Fe_{0.36}Mo_{0.64}S_2$ sample (Figure 2e). Instead, a new diffraction peak at ~17° may

correspond to the 2nd-order reflections from the (002) plane of $Fe_xMo_{1-x}S_2$. A similar

phenomenon was observed in Ni-doped MoS_2 [20]. The diffraction peaks from 30° to

60° can be indexed to MoS_2, demonstrating a similar atomic arrangement between

$Fe_{0.36}Mo_{0.64}S_2$ and MoS_2. The Fourier-transform infrared (FTIR) spectrum of $Fe_xMo_{1-x}S_2$

shows peaks at 619-766 cm^{-1}, assigning to the Fe-S stretching vibrations (Figure 2f) [30,

31]. The absorption band between 1113 cm $^{-1}$ and 1630 cm $^{-1}$ may be ascribed to the

stretching vibrations of the hydroxyl group and Mo-S vibrations [32, 33].

The images recorded *via* SEM and STEM reveal that the doping of Fe in MoS_2 does

not affect the nanosheet morphology (Figure 3a-b). The HRTEM image shows distinct

ripples and corrugations with a layer distance of 0.67 nm corresponding to the (002)

crystalline plane of $Fe_{0.36}Mo_{0.64}S_2$ (Figure 3c), which is slightly larger than that of pristine

MoS_2 (~0.62 nm). The observation of similarly enlarged interlayer spacing has been

reported in Ni-doped MoS_2 [20]. There are no nanoparticles or large clusters appearing in

the HRTEM images, which rules out any possible formation of ferrous sulfide. Rather,

the spherical aberration-corrected HRTEM image shows small white dots uniformly

dispersed in the MoS_2 matrix, which could be interpreted as single Fe atoms. Some of

them are tagged by red cycles (Figure 3d). The low contrast in the image is due to the

similar atomic weight of Fe and Mo atoms. The uniform distribution of Fe, as well as Mo

and S atoms, in the $Fe_xMo_{1-x}S_2$ catalyst was further demonstrated by energy-dispersive X-

ray spectroscopic elemental mapping in HAADF-STEM images (Figure 3e-h).

3.2 Catalytic performance of $Fe_xMo_{1-x}S_2$

The degradation of organic pollutants was used to verify the catalytic performance of

different $Fe_xMo_{1-x}S_2$ catalysts for sulfite activation. We first studied the effect of Fe

content on the catalytic activity of $Fe_xMo_{1-x}S_2$ by recording the rates of PPA degradation.

Unambiguously, the doping of single Fe ions significantly enhances the catalytic activity

of $Fe_xMo_{1-x}S_2$ for sulfite activation with obtained maximum rate constants for $x = 0.36$

(Figure 4a). Further increasing the Fe content resulted in lower rate constants. This

indicates the important roles of both Fe and Mo for synergistic catalysis.

In control experiments, we studied the individual role of $Fe_{0.36}Mo_{0.64}S_2$ and sulfite for PPA degradation. With $Fe_{0.36}Mo_{0.64}S_2$ in the absence of sulfite, only ~8.9% of PPA was removed under the same conditions, which may be attributed to the adsorption of PPA onto $Fe_{0.36}Mo_{0.64}S_2$ (Figure 4b). In the presence of only sulfite, the situation is even worse, as negligible PPA degradation was observed. In contrast, $Fe_{0.36}Mo_{0.64}S_2$/sulfite system results in 90.0% of PPA degradation after only 30 min reaction, confirming the high activity of $Fe_xMo_{1-x}S_2$ for sulfite activation, which generates ROS to degrade PPA (Figure 4b). For comparison, we studied similar catalysts for sulfite activation and the associated PPA degradation. In the Fe_2O_3/sulfite, MoO_3/sulfite, MoS_2/sulfite system, the PPA degradation efficiencies after 30 min were 65.8%, 46.6%, 32.2%, respectively, all much lower than the $Fe_{0.36}Mo_{0.64}S_2$/sulfite system (Figure 4b). These results further highlight that $Fe_xMo_{1-x}S_2$ is a highly efficient catalyst to activate sulfite for the degradation of organic pollutants in water.

It has been reported that dissolved metal cations can also activate sulfite in a homogeneous process. To examine the role of any homogeneous process, we studied the leaching of Fe and Mo ions into the solution and their activity for sulfite activation. It was observed that Fe and Mo were gradually released from the $Fe_{0.36}Mo_{0.64}S_2$ catalyst into the solution during the reaction (Figure S3a). The possible homogeneous sulfite activation by the released Fe or Mo ion was evaluated using the respective Fe or Mo concentration observed at the start and the end of the reaction. The highest PPA degradation efficiency (~19.8%) was observed in the Fe/sulfite system using the maximum iron concentration at the end of the reaction (Figure S3b), which is significantly lower than the PPA degradation efficiency (90.0%) observed in

$Fe_{0.36}Mo_{0.64}S_2$/sulfite system. Thus, the homogeneous sulfite activation in $Fe_xMo_{1-x}S_2$/sulfite system has only a small contribution to PPA degradation compared to heterogeneous sulfite activation.

3.3 Effect of reaction parameters

3.3.1 Effect of initial pH

The PPA degradation in $Fe_{0.36}Mo_{0.64}S_2$/sulfite at initial pH values of 3.0, 4.0, 5.0, 6.0, 7.0 and 8.0 was investigated (Figure 5a, Figure S4). Highest PPA degradation rate was observed at pH 4.0 with an initial degradation rate r_0 of 0.46 μM/min. At initial pH of 3.0, 5.0, 6.0, 7.0 and 8.0, the final PPA degradation efficiency was 55.6%, 89.8%, 88.0%, 34.2% and 34.5%, respectively. The PPA degradation rate increased from 0.17 μM/min to 0.46 μM/min when the initial pH decreased from 8.0 to 4.0. A further decrease of initial pH to 3.0 resulted in a decrease in PPA degradation rate to 0.27 μM/min. In general, the sulfite activation by $Fe_xMo_{1-x}S_2$ is more efficient at acidic conditions than at neutral and alkaline conditions.

The role of initial pH was further revealed by the relationship between the initial PPA degradation rate and distribution of HSO_3^- species at different pH. Na_2SO_3 has two major forms, i.e. HSO_3^-/SO_3^{2-} (pK_a=7.2), depending on pH (Figure S5). HSO_3^- is the dominant species at acidic conditions whereas SO_3^{2-} species dominate at alkaline conditions. An increase of pH from 4.0 to 8.0 leads to a decrease of HSO_3^- concentration, which is in line with the decrease of PPA degradation efficiency and initial degradation rate observed in this work (Figure 5a). A decrease of pH from 4.0 to 3.0 resulted in the formation of SO_2 in solution which may escape into the gas phase. Subsequently, the HSO_3^- concentration in aqueous solution will decline. This speculation

13

is supported by the observed decrease in reaction rate and PPA degradation efficiency when the initial pH dropped from 4.0 to 3.0 (Figure 5a). Thus, the PPA degradation in $Fe_xMo_{1-x}S_2$/sulfite system is attributed to the activation of HSO_3^- by $Fe_xMo_{1-x}S_2$ catalyst.

In addition, the change of Na_2SO_3 concentration was monitored during the reaction at different pH values. (Figure S6). The percentage of remaining Na_2SO_3 was 2.7%, 0.1%, 0.6%, 25.3%, 44.9%, 68.8% at initial pH of 3.0, 4.0, 5.0, 6.0, 7.0, 8.0, respectively. High Na_2SO_3 consumption at low pH is in agreement with the high PPA removal in $Fe_xMo_{1-x}S_2$/sulfite system. The highest Na_2SO_3 consumption rate at pH 4.0 resulted in the highest PPA degradation efficiency. A relatively low PPA degradation efficiency but high Na_2SO_3 consumption rate was observed at pH 3.0. This is in agreement with the fact that parts of Na_2SO_3 in solution may transform to SO_2 which is released into gas phase at pH 3.0.

3.3.2　Effect of sulfite/$Fe_xMo_{1-x}S_2$ dosage and dissolved oxygen

The effect of sulfite dosage on PPA degradation in $Fe_xMo_{1-x}S_2$/sulfite system was investigated (Figure 5a). When the concentration of Na_2SO_3 in the system increased from 0.1 mM to 1 mM, the PPA degradation efficiency increased from 43.2% to 90.0% and the pseudo-1st-order rate constant increased from 0.024 min^{-1} to 0.108 min^{-1}. Further increase in Na_2SO_3 concentration from 1 mM to 2 mM led to a decrease in PPA degradation efficiency and pseudo-1st-order rate constant to 79.8% and 0.057 min^{-1}, respectively. Although Na_2SO_3 is important for radical generation in $Fe_xMo_{1-x}S_2$/sulfite systems, excessive HSO_3^- may react with $SO_5^{\bullet-}$ radicals (see below). Thus HSO_3^- may compete with PPA for $SO_5^{\bullet-}$ radicals which inhibits the PPA degradation. Also, $SO_5^{\bullet-}$ is identified as an important ROS generated in the system (see below). $SO_5^{\bullet-}$ is generated

14

via the oxidation of $SO_3^{\bullet-}$ by dissolved oxygen. The change of dissolved oxygen was monitored during the reaction. It was found that the dosage of sulfite at the start of the reaction can consume dissolved oxygen due to the reductive property of sulfite (Figure S8). Thus, excessive sulfite dosage could consume dissolved oxygen rapidly, inhibiting the formation of $SO_5^{\bullet-}$ in the system. Subsequently, the decrease of the pseudo-1st-order rate constant with excessive sulfite dosage was observed.

When $Fe_{0.36}Mo_{0.64}S_2$ dosage was increased from 0.01 g/L to 0.1 g/L, the PPA degradation efficiency increased from 13.4% to 90.0% and the pseudo-1st-order rate constant increased from 0.0069 min^{-1} to 0.108 min^{-1} (Figure 5c). Further increase of the catalyst dosage from 0.1 g/L to 0.2 g/L did not lead to an increase in PPA degradation efficiency, which is probably due to the saturation of the active catalytic sites under the studied experimental conditions. Thus, 0.1 g/L $Fe_{0.36}Mo_{0.64}S_2$ was chosen as an optimum dosage and used throughout the experiment.

Moreover, the PPA degradation in $Fe_{0.36}Mo_{0.64}S_2$/sulfite-Ar, $Fe_{0.36}Mo_{0.64}S_2$/sulfite-O_2 and $Fe_{0.36}Mo_{0.64}S_2$/sulfite-air systems were tested to investigate the effect of dissolved oxygen on sulfite activation (Figure 5d). The reaction solution was bubbled with Ar or O_2 gas for at least 1 h to obtain O_2-free or O_2-saturated environment. Only ~10% of PPA removal was observed in the $Fe_{0.36}Mo_{0.64}S_2$/sulfite-Ar system, which may be due to the PPA adsorption onto the catalyst. A higher initial degradation rate of PPA was observed in the $Fe_xMo_{1-x}S_2$/sulfite-O_2 system than in $Fe_xMo_{1-x}S_2$/sulfite-air system, which further demonstrates the essential role of dissolved oxygen for PPA degradation. Dissolved oxygen plays an important role during the oxidation of $SO_3^{\bullet-}$ to $SO_5^{\bullet-}$ radical, which influences PPA degradation in $Fe_xMo_{1-x}S_2$/sulfite system (see below).

15
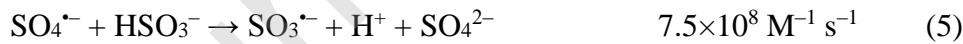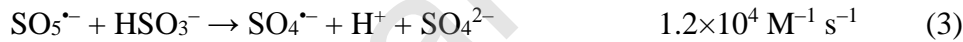
3.4 Mechanism for sulfite activation by $Fe_xMo_{1-x}S_2$

3.4.1   Identification of reactive radicals

In our system, several radicals could be responsible for the pollutant degradation, including hydroxyl radical ($HO^\bullet$) and oxysulfur radicals (e.g. $SO_3^{\bullet-}$, $SO_4^{\bullet-}$ and $SO_5^{\bullet-}$). We conducted radical quenching experiments to investigate which radical plays the major role (Figure 6a, Test S1). The addition of 10 mM *tert*-butanol as a $HO^\bullet$ scavenger has little influence on the PPA degradation, indicating negligible contribution of $HO^\bullet$ to PPA degradation. Subsequently, we employed ethanol as a scavenger for $SO_4^{\bullet-}$. The addition of a high concentration of ethanol (50 and 100 mM) slightly decreases the PPA degradation efficiency (from 90% to 82% and 73%, respectively). This suggests that $SO_4^{\bullet-}$ contributes to PPA degradation but is not the major ROS. It has been shown that aniline is an effective scavenger for $SO_5^{\bullet-}$ [34]. In the $Fe_{0.36}Mo_{0.64}S_2$/sulfite system, the presence of a small concentration of aniline (0.5 mM) can greatly inhibit the PPA degradation, indicating $SO_5^{\bullet-}$ is the major ROS. The addition of 10 mM aniline decreases the PPA degradation efficiency to 10.8%, which is similar to the value of ~8.9% of PPA adsorption onto $Fe_{0.36}Mo_{0.64}S_2$ shown in Figure 4b.

To further identify the generated radicals, 5,5-dimethyl-1-pyrroline N-oxide (DMPO) trapped electron spin resonance experiments were conducted. The signal of $DMPO-SO_3^{\bullet-}$ (a_N=14.7G, a_H=16.1G) was observed in the $Fe_xMo_{1-x}S_2$/sulfite system after 1 min reaction (Figure 6b). It should be noted that DMPO cannot trap $SO_5^{\bullet-}$ to provide an observable signal even if $SO_5^{\bullet-}$ existed in the system [35]. Since the radical quenching experiments confirm $SO_5^{\bullet-}$ rather than $SO_3^{\bullet-}$ is responsible for PPA degradation, it is suggested that the oxidation of $SO_3^{\bullet-}$ by dissolved oxygen to $SO_5^{\bullet-}$ takes place. Indeed,

16

the rate constant for this oxidation process is very high (reaction 1). This is supported by

the fact that no PPA degradation was observed in the $Fe_{0.36}Mo_{0.64}S_2$/sulfite-Ar system

(Figure 5d). Since $SO_3^{\bullet-}$ cannot transform to $SO_5^{\bullet-}$ under inert conditions, no PPA

degradation was observed. This also confirms the oxidation of PPA by $SO_3^{\bullet-}$ is

negligible. The generated $SO_3^{\bullet-}$ was readily oxidized to $SO_5^{\bullet-}$ by dissolved oxygen with

a high rate constant of 2.5×10^9 M^{-1} s^{-1} (reaction 1). Subsequently, $SO_5^{\bullet-}$ reacts with

HSO_3^- (sulfite exists as HSO_3^- at the studied pH 4) to produce $SO_3^{\bullet-}$ and $SO_4^{\bullet-}$ (reactions

2&3). Meanwhile, the internal electron transfer of $SO_5^{\bullet-}$ can lead to the formation of

$SO_4^{\bullet-}$ (reaction 4). The generated $SO_4^{\bullet-}$ reacts with HSO_3^- to produce $SO_3^{\bullet-}$ (reaction 5).

Eventually, the cycle of oxysulfur radicals $SO_x^{\bullet-}$ involving $SO_3^{\bullet-}$, $SO_4^{\bullet-}$ and $SO_5^{\bullet-}$ is

established [2].

$$SO_3^{\bullet-} + O_2 \rightarrow SO_5^{\bullet-} \qquad\qquad 2.5\times10^9\ M^{-1}\ s^{-1} \qquad (1)$$

$$SO_5^{\bullet-} + HSO_3^- \rightarrow SO_3^{\bullet-} + HSO_5^- \qquad\qquad \leq3\times10^5\ M^{-1}\ s^{-1} \qquad (2)$$

$$SO_5^{\bullet-} + HSO_3^- \rightarrow SO_4^{\bullet-} + H^+ + SO_4^{2-} \qquad\qquad 1.2\times10^4\ M^{-1}\ s^{-1} \qquad (3)$$

$$SO_5^{\bullet-} + SO_5^{\bullet-} \rightarrow 2SO_4^{\bullet-} + O_2 \qquad\qquad 2.2\times10^8\ M^{-1}\ s^{-1} \qquad (4)$$

$$SO_4^{\bullet-} + HSO_3^- \rightarrow SO_3^{\bullet-} + H^+ + SO_4^{2-} \qquad\qquad 7.5\times10^8\ M^{-1}\ s^{-1} \qquad (5)$$

It can be concluded from the radical quenching and electron spin resonance

experiments that $SO_5^{\bullet-}$ is the major ROS responsible for PPA degradation. $SO_4^{\bullet-}$ also

contributes to PPA degradation, whereas the contribution from $HO^{\bullet-}$ is negligible.

Furthermore, competitive kinetics was used to determine the reaction rate constant

between $SO_5^{\bullet-}$ and PPA ($k_{PPA,\ SO_5\bullet-}$). $k_{PPA,SO5\bullet-}$ was determined in Fe(III)/sulfite system

which generates $HO^{\bullet}$, $SO_4^{\bullet-}$ and $SO_5^{\bullet-}$. The 2nd-order rate constant between ethanol and

HO$^\bullet$ or SO$_4{}^{\bullet-}$ is very high ($k_{EtOH, HO\bullet}$ = 1.8−2.8×10^9 M^{-1} s^{-1}, and $k_{EtOH, SO4\bullet-}$ =

1.6−6.2×10^7 M^{-1} s^{-1}), thus SO$_4{}^{\bullet-}$ and HO$^\bullet$ can both be quenched with ethanol. On the

other hand, the rate constant between ethanol and SO$_5{}^{\bullet-}$ is lower than 1×10^3 M^{-1} s^{-1}.

Thus, the addition of an appropriate amount of ethanol can quench all HO$^\bullet$ and SO$_4{}^{\bullet-}$ in

the Fe(Ⅲ)/sulfite system leaving SO$_5{}^{\bullet-}$ as the only radical (Figure S10a, reaction S1-3).

The slope of ln([PPA]$_0$/[PPA]$_t$) plotted ln([AN]$_0$/[AN]$_t$) is 1.854 and the calculated value

of $k_{PPA,SO5\bullet-}$ was as large as (1.1±0.6)×10^7 M^{-1} s^{-1} (Figure S10b).

3.4.2 Identification of catalytic sites

The possible catalytic role of Fe and Mo sites for sulfite activation was verified by

electrochemical analysis and high-resolution XPS spectra. Electron transfer between

Fe$_x$Mo$_{1-x}$S$_2$ and sulfite in solution is evidenced by the observed corrosion current

(8.1×10^{-8} A), which was obtained by fitting the Tafel curves recorded at Fe$_{0.36}$Mo$_{0.64}$S$_2$

(Figure 7a). This electron transfer process evidences the catalytic activity of Fe$_x$Mo$_{1-x}$S$_2$

for sulfite activation. The cyclic voltammograms of MoS$_2$ show two reduction peaks in

the cathodic scan (Figure 7b). The reduction peak at -0.24 V could result from the

reduction of Mo^{6+} to Mo^{5+}, whereas the peak at -0.85 may result from the reduction of

Mo^{5+} to Mo^{4+}. For Fe$_{0.36}$Mo$_{0.64}$S$_2$, a similar cathodic peak from the reduction of Mo^{6+} to

Mo^{5+} was observed whereas the cathodic peak from the reduction of Mo^{5+} to Mo^{4+} was

enlarged. It is interesting to note that negligible oxidation peaks were observed with

MoS$_2$ indicating Mo has very low redox reactivity. In contrast, two oxidation peaks at -

0.47 and -0.02 were observed with Fe$_{0.36}$Mo$_{0.64}$S$_2$, which most likely resulted from the

oxidation of Mo^{4+} to Mo^{5+} and Mo^{5+} to Mo^{6+}, respectively (Figure 7b). The results

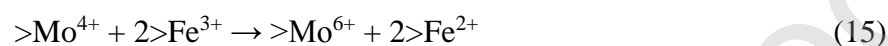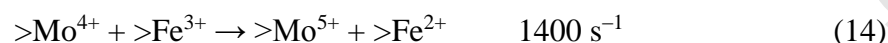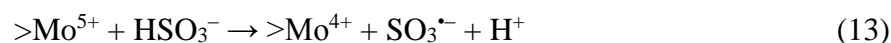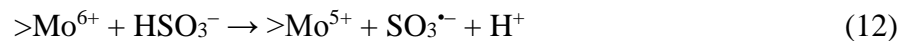indicate the confined single Fe atoms can activate the redox activity of Mo atoms which

18

may promote the intrinsic catalytic activities of MoS_2. This is in line with the observed perturbation of the electronic structure of MoS_2 upon Fe doping (see above).

The catalytic role of Fe and Mo sites was further demonstrated by the similar binding energy in XPS spectra before and after catalysis (Figure S11-12). $>Fe^{2+}$ ($>$ denotes the catalyst surface) can complex with HSO_3^- to form $>FeHSO_3^+$ (reaction 6), which is oxidized by dissolved oxygen or ROS (denoted as [O]) to form $>FeSO_3^+$ complex (reaction 7). The electron transfer within $>FeSO_3^+$ complex leads to the formation of $>Fe^{2+}$ and $SO_3^{•-}$ (reaction 8). Thus, a Fe^{2+}/Fe^{3+} redox cycle is established [2].

$$>Fe^{2+} + HSO_3^- \rightarrow >FeHSO_3^+ \qquad\qquad 10^4 \text{ M}^{-1} \text{ s}^{-1} \qquad\qquad (6)$$

$$2>FeHSO_3^+ + [O] \rightarrow 2>FeSO_3^+ + H_2O \qquad 1.69\times10^3 \text{ M}^{-1} \text{ s}^{-1} \qquad (7)$$

$$>FeSO_3^+ \leftrightarrow >Fe^{2+} + SO_3^{•-} \qquad\qquad\qquad 0.19 \text{ M}^{-1} \text{ s}^{-1} \qquad\qquad (8)$$
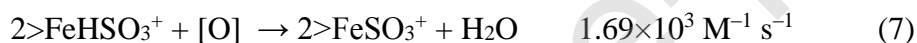
For the Mo catalytic sites, $>Mo^{4+}$ can be oxidized by dissolved oxygen and ROS to $>Mo^{5+}$ or $>Mo^{6+}$ (reaction 9-10). The electron transfer from sulfite to $>Mo^{6+}$ leads to the formation of $>Mo^{4+}$, $>Mo^{5+}$ and $SO_3^{•-}$ (reaction 11-12). The electron transfer from sulfite to the generated $>Mo^{5+}$ may produce $>Mo^{4+}$ and $SO_3^{•-}$ *via* reaction 13. The production of H^+ ions *via* reaction 11-13 was indicated by the decreased pH along the reaction course (Figure S13). Eventually, the Mo redox cycle between 4+, 5+ and 6+ was established. A similar $Mo^{4+}/Mo^{5+}/Mo^{6+}$ redox cycle was also reported for sulfite oxidase catalyzed sulfite oxidation (Figure S1) [36, 37].

$$2>Mo^{4+} + [O] + H^+ \rightarrow 2>Mo^{5+} + OH^- \qquad\qquad\qquad (9)$$

19

$$>Mo^{4+} + [O] + H^+ \rightarrow >Mo^{6+} + OH^- \qquad (10)$$

$$>Mo^{6+} + 2HSO_3^- \rightarrow >Mo^{4+} + 2SO_3^{\bullet-} + 2H^+ \qquad (11)$$

$$>Mo^{6+} + HSO_3^- \rightarrow >Mo^{5+} + SO_3^{\bullet-} + H^+ \qquad (12)$$

$$>Mo^{5+} + HSO_3^- \rightarrow >Mo^{4+} + SO_3^{\bullet-} + H^+ \qquad (13)$$

$$>Mo^{4+} + >Fe^{3+} \rightarrow >Mo^{5+} + >Fe^{2+} \qquad 1400 \ s^{-1} \qquad (14)$$

$$>Mo^{4+} + 2>Fe^{3+} \rightarrow >Mo^{6+} + 2>Fe^{2+} \qquad (15)$$
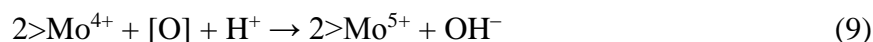
The interaction between the Fe and Mo catalytic sites within $Fe_xMo_{1-x}S_2$ catalyst may also occur to promote synergistic catalysis. Electron transfer within 2D nanosheets is speculated to be very fast compared to that across stacked inter-sheets [38]. Thus, fast electron transfer between the Fe and Mo catalytic sites is expected. The electron transfer from $>Mo^{4+}$ to $>Fe^{3+}$ leads to the formation of $>Mo^{5+}$, $>Mo^{6+}$ and $>Fe^{2+}$ (reaction 14-15), which is confirmed by previous works using paramagnetic resonance, electron-electron double resonance, and X-ray absorption spectroscopy [37, 39]. Thus, the Fe^{2+}/Fe^{3+} and $Mo^{4+}/Mo^{5+}/Mo^{6+}$ redox cycle could interact and work collaboratively during catalytic sulfite activation, mimicking sulfite oxidase [36, 37]. It should be noted that both the establishment of and the interaction between Fe and Mo redox cycles need dissolved oxygen in the reaction solution as a prerequisite. Also, dissolved oxygen plays an essential role in the transformation of $SO_3^{\bullet-}$ to $SO_5^{\bullet-}$ which is responsible for PPA degradation (see above).

3.4.3 Degradation pathway of PPA

In order to determine the degradation pathway of PPA in Fe$_x$Mo$_{1-x}$S$_2$/sulfite system, the degradation products of PPA were determined by LC-MS. Six degradation products (DPs) were observed. The MS spectra are shown in Figure S14. The transformation of SO$_x^{\bullet-}$ to HO$^{\bullet}$ was confirmed by our ESR results (Figure S15), thus PPA can be attacked by both HO$^{\bullet}$ and SO$_x^{\bullet-}$ radicals. The first degradation pathway involves the bond cleavage between the naphthalene ring and the lateral chain of the PPA molecule, leading to the formation of 1-naphtol and hydroxylated amine [40]. The formed 1-naphtol could undergo HO$^{\bullet}$ and SO$_x^{\bullet-}$ attack to form DPs (m/z 160 and m/z 239). The second degradation pathway involves the substitution of the naphthalene ring by HO$^{\bullet}$ with the formation of DPs (m/z 276 and m/z 292). Also, the total organic carbon (TOC) of the system during the reaction was monitored (Figure S16). The TOC decreased by 10.0% after 60 minutes of reaction, which is in line with the PPA degradation in the reported sulfite systems [4]. Many radical substitution products were observed using LC-MS, indicating substitution reactions are responsible for PPA degradation. Despite PPA degradation the percentage of mineralization was low, which is in line with the negligible contribution of HO$^{\bullet}$ for PPA degradation. In conclusion, the degradation pathway of PPA in the Fe$_x$Mo$_{1-x}$S$_2$/sulfite system is proposed (Figure 8).

3.4.4 DFT calculations

To further investigate the mechanism of sulfite activation on the surface of Fe$_x$Mo$_{1-x}$S$_2$, we carried out first principles calculations of sulfite adsorbed on Fe$_x$Mo$_{1-x}$S$_2$. The absorption energy of sulfite on the surface of Fe$_x$Mo$_{1-x}$S$_2$ was calculated by

$$\Delta E = E_{\text{Fe}_x\text{Mo}_{1-x}\text{S}_2+\text{Na}_2\text{SO}_3} - E_{\text{Fe}_x\text{Mo}_{1-x}\text{S}_2} - E_{\text{Na}_2\text{SO}_3} \qquad (16)$$

21

where $E_{Fe_xMo_{1-x}S_2+Na_2SO_3}$, $E_{Fe_xMo_{1-x}S_2}$ and $E_{Na_2SO_3}$ are the total energies of substrate

with adsorbate, substrate, and free molecule, respectively. Four configurations of $Fe_xMo_{1-x}S_2$ ($x = 0$, 0.22, 0.36 and 0.51) were considered here. The calculated absorption energy of

sulfite on $Fe_xMo_{1-x}S_2$ increased with Fe content (x), implying the increasing interaction

with the doping of Fe (Table S2). Furthermore, the charge transfer between sulfite and

$Fe_xMo_{1-x}S_2$ was examined. The charge density difference of sulfite adsorbed on the

surface of $Fe_xMo_{1-x}S_2$ was calculated by

$$\Delta\rho = \rho_{Fe_xMo_{1-x}S_2+Na_2SO_3} - \rho_{Fe_xMo_{1-x}S_2} - \rho_{Na_2SO_3} \qquad (17)$$

where $\rho_{Fe_xMo_{1-x}S_2+Na_2SO_3}$, $\rho_{Fe_xMo_{1-x}S_2}$ and $\rho_{Na_2SO_3}$ are the total charge densities of

substrate with adsorbate, substrate, and free molecule, respectively. The top and side

views of charge density difference of sulfite on MoS_2 and $Fe_{0.36}Mo_{0.64}S_2$ are shown in

Figure 9a-d. The quantitative atomic charge analysis following Bader's atom-in-molecule

approach [41] demonstrates that the charge transfer from sulfite to MoS_2 and

$Fe_{0.36}Mo_{0.64}S_2$ are 0.226 electrons and 0.363 electrons, respectively, indicating the

increasing activity of $Fe_xMo_{1-x}S_2$ with the doping of Fe. However, it should be noted that

too strong binding of sulfite will induce poisoning of the active site while too weak

binding of sulfite will make it harder to effectively activate the adsorbed sulfite

molecules. On the basis of the above investigations, an optimal Fe-doped concentration to

maximize the catalytic performance of $Fe_xMo_{1-x}S_2$ should exist, which is 0.36 as

demonstrated by the highest rate constant observed for $Fe_{0.36}Mo_{0.64}S_2$ catalyst (Figure 9e).

On the basis of the above investigations, we propose a synergistic Mo-Fe catalysis

mechanism for the $Fe_xMo_{1-x}S_2$ catalyzed sulfite activation for ROS generation (Figure

10). The $Fe_xMo_{1-x}S_2$ with $x=0.36$ resulted in the optimum adsorption energy and charge

transfer between sulfite and the catalyst, which allows the highest catalytic sulfite activation. The Fe or Mo sites can activate sulfite individually *via* the Fe^{2+}/Fe^{3+} or $Mo^{4+}/Mo^{5+}/Mo^{6+}$ redox cycle. More importantly, the synergistic catalysis involving the Fe and Mo sites play an essential role as evidenced by the maximum catalytic performance of $Fe_xMo_{1-x}S_2$ with the optimum Fe/Mo ratio. The redox reaction between Fe and Mo sites favor the turnover of Fe or Mo redox cycle, and the atomically dispersed Fe sites in MoS_2 support shall maximize the utilization of single Fe atoms. The dissolved oxygen plays an important role in the metal redox cycle and radical transformation cycle, since little oxidative power of $Fe_xMo_{1-x}S_2$/sulfite system was observed under O_2-free conditions.

3.5 Potential practical application of $Fe_xMo_{1-x}S_2$/sulfite system

In order to investigate the reusability of the $Fe_xMo_{1-x}S_2$ catalyst, the catalyst was recycled five times and the catalytic performance was evaluated (Figure 11a). The results showed that the degradation efficiency of PPA decreased gradually with the catalyst reuse cycles, from 90.0% when used for the first time to 62.1% in the fifth cycle. Notably, $Fe_xMo_{1-x}S_2$ shows almost the same HRTEM images, XRD patterns and FTIR spectrum before and after catalysis, demonstrating its structural stability during the reaction (Figure S17). Hence, the observed decrease in catalytic activity may originate from the leaching of Fe and Mo from the $Fe_xMo_{1-x}S_2$ catalyst after the reaction. In addition, the surface of the catalyst is likely to adsorb the degradation products of PPA from the previous cycle. It may be difficult to remove them completely by washing with ultrapure water and ethanol. These impurities may block the active sites on the surface of the catalyst and reduce its reactivity for sulfite activation.

In order to further test the potential application of $Fe_xMo_{1-x}S_2$ in other advanced oxidation processes, PPA degradation in $Fe_xMo_{1-x}S_2$/persulfate, $Fe_xMo_{1-x}S_2$/peroxymonosulfate and $Fe_xMo_{1-x}S_2$/H$_2$O$_2$ systems was investigated (Figure 11b). The $Fe_{0.36}Mo_{0.64}S_2$/PS and $Fe_{0.36}Mo_{0.64}S_2$/PMS systems can degrade PPA completely within 20 minutes with different reaction rates. This may be due to the different molecular structures of PS and PMS. The former is symmetrical, while the latter is asymmetrical. The difference in bond dissociation energy between them may also be one of the reasons. The degradation rates of PPA in the $Fe_{0.36}Mo_{0.64}S_2$/sulfite system and the $Fe_{0.36}Mo_{0.64}S_2$/H$_2$O$_2$ system after 30 min reaction were 90.0% and 62.2%, respectively. The relatively low degradation efficiency of PPA in the $Fe_xMo_{1-x}S_2$/H$_2$O$_2$ system may be due to the lack of optimization of H$_2$O$_2$ dosage in the study. Among the three sulfur systems, the PPA degradation efficiency is higher in persulfate and peroxymonosulfate systems than in the sulfite system. On the other hand, sulfite is cheaper and more environmentally friendly than persulfate and peroxymonosulfate. Also, sulfite as a waste from power generation plants can be reused for this application [42, 43].

In order to explore the potential application of $Fe_xMo_{1-x}S_2$/sulfite systems in the degradation of various organic pollutants, seven target pollutants were studied, i.e. atenolol, estriol, orange II, indigo, benzoic acid, methylene blue and fluoxetine (Figure 11c). Similar to PPA, atenolol is a beta-blocker used in the treatment of cardiovascular diseases and is an emerging organic pollutant difficult to remove with conventional sewage treatment processes; estriol is an estrogen, which interferes with the endocrine system of organisms in the water environment; benzoic acid is an aromatic compound with stable structure and high toxicity, usually found in industrial wastewater; orange II,

indigo and methylene blue are common dyes in printing and dyeing wastewaters with poor biodegradability. The results showed that the removal rates of estriol, atenolol, orange II, indigo, benzoic acid, methylene blue and fluoxetine were 51.7%, 23.7%, 35.7%, 89.5%, 75.5%, 61.4% and 80.5% respectively. Although different extents of degradation were observed depending on the structures of various pollutants, the results suggest that the $Fe_xMo_{1-x}S_2$/sulfite system is a versatile platform for degradation of organic pollutants.

In order to investigate the application of $Fe_xMo_{1-x}S_2$/sulfite system in a real world environment, water was collected from East Lake (Wuhan, China), filtered with 0.45 μm membrane and used in the experiment. The water quality of the East Lake is shown in Table S3. The $Fe_xMo_{1-x}S_2$/sulfite system achieves almost the same PPA removal efficiency after 30 min reaction in real water as in ultra-pure water, confirming the applicability of the system under natural environmental conditions (Figure 11d). The reaction rate in real lake water is slower than in ultra-pure water, which may be due to the competition of ROS between PPA and the abundant dissolved organic compounds, ions or other substances in real lake water.

Although the $Fe_xMo_{1-x}S_2$/sulfite system shows great potential in practical application, several issues need to be resolved before its real engineering application. The reactivity of the $Fe_xMo_{1-x}S_2$/sulfite system should be further improved at near neural conditions to avoid acidification and post-neutralization of the treated water. The recovery of the catalyst using filtration will be a problem in real applications, and hybrid magnetic catalyst is thus advised for facile magnetic recovery. Mineralization of organic pollutants by the $Fe_xMo_{1-x}S_2$/sulfite system is relatively low, and efforts towards transformation of

25

$SO_5^{\bullet-}$ to more powerful $HO^{\bullet}$ radicals in some cases is thus advised. Finally, the catalyst synthesis need to be further optimized and scaled-up to lower the cost of the catalyst for mass production.

4. Conclusions

We have demonstrated that single Fe atoms confined in 2D MoS_2 support can mimic sulfite oxidase enzyme for highly efficient sulfite activation. The $Fe_xMo_{1-x}S_2$ catalysts were successfully synthesized *via* a one-pot hydrothermal method and thoroughly characterized. The highest PPA degradation rate was observed at pH 4.0. The optimum sulfite and $Fe_xMo_{1-x}S_2$ dosages were 1 mM and 0.1 g/L, respectively. Radical quenching and electron spin resonance experiments demonstrate that $SO_5^{\bullet-}$ is the major radical responsible for PPA degradation. The $Fe_xMo_{1-x}S_2$ catalysts prepared in this work provides dual Fe-Mo catalytic sites with synergistic catalysis to achieve high catalytic performance. The 2D MoS_2 support confines single Fe atoms as highly reactive catalytic sites, and the catalytic activity of MoS_2 support can be triggered *via* Fe doping. Furthermore, the strong interaction between Fe and Mo atoms within the 2D structure can enhance the overall catalytic performance *via* synergistic catalysis. The highest catalytic performance of the $Fe_{0.36}Mo_{0.64}S_2$ catalyst was interpreted by density functional theory calculation *via* the adsorption energy of sulfite on the catalyst surface. The biomimetic mechanism based on the interaction of single-atom dual catalytic sites proposed in our work shall shed light on the development of other biomimetic single-atom dual-site catalysts in the future.

Declaration of interests

The authors declare that they have no known competing financial interests or personal relationships that could have appeared to influence the work reported in this paper.

Li-Zhi Huang: Conceptualization, Methodology, Writing - Original Draft, Project administration, Funding acquisition, Investigation

Xiuli Wei: Validation, Investigation

Enlai Gao: Formal analysis

Chunbo Zhang: Formal analysis

Xin-Ming Hu: Writing - Review & Editing

Yiqun Chen, Supervision, Funding acquisition

Zizheng Liu: Supervision, Funding acquisition

Nicolas Finck: Formal analysis

Johannes Lützenkirchen: Writing - Review & Editing

Dionysios D. Dionysiou: Writing - Review & Editing

Acknowledgements

Additional information

Supplementary Information associated with this article can be found in the online version.

References

[1] A.T.S. Wyse, M. Grings, M. Wajner, G. Leipnitz, The role of oxidative stress and bioenergetic dysfunction in sulfite oxidase deficiency: Insights from animal models, Neurotoxicity Research, 35 (2019) 484-494.

[2] D. Zhou, L. Chen, J. Li, F. Wu, Transition metal catalyzed sulfite auto-oxidation systems for oxidative decontamination in waters: A state-of-the-art minireview, Chemical Engineering Journal, 346 (2018) 726-738.

[3] L. Chen, M. Tang, C. Chen, M. Chen, K. Luo, J. Xu, D. Zhou, F. Wu, Efficient bacterial inactivation by transition metal catalyzed auto-oxidation of sulfite, Environmental Science & Technology, 51 (2017) 12663-12671.

[4] Y.Q. Chen, M.Y. Li, Y. Tong, Z.Z. Liu, L.P. Fang, Y. Wu, Z. Fang, F. Wu, L.Z. Huang, Radical generation via sulfite activation on $NiFe_2O_4$ surface for estriol removal: Performance and mechanistic studies, Chemical Engineering Journal, 368 (2019) 495-503.

[5] H. Zhang, G. Liu, L. Shi, J. Ye, Single-atom catalysts: Emerging multifunctional materials in heterogeneous catalysis, Advanced Energy Materials, 8 (2018).

[6] X.N. Li, X. Huang, S.B. Xi, S. Miao, J. Ding, W.Z. Cai, S. Liu, X.L. Yang, H.B. Yang, J.J. Gao, J.H. Wang, Y.Q. Huang, T. Zhang, B. Liu, Single cobalt atoms anchored on porous N-doped graphene with dual reaction sites for efficient Fenton-like catalysis, Journal of the American Chemical Society, 140 (2018) 12469-12475.

29

[7] Y. Yin, L. Shi, W. Li, X. Li, H. Wu, Z. Ao, W. Tian, S. Liu, S. Wang, H. Sun, Boosting Fenton-like reactions *via* single atom fe catalysis, Environmental Science & Technology, (2019).

[8] Z. Guo, Y. Xie, J. Xiao, Z.-J. Zhao, Y. Wang, Z. Xu, Y. Zhang, L. Yin, H. Cao, J. Gong, Single-atom Mn–N_4 site-catalyzed peroxone reaction for the efficient production of hydroxyl radicals in an acidic solution, Journal of the American Chemical Society, 141 (2019) 12005-12010.

[9] R.M. Garrett, J.L. Johnson, T.N. Graf, A. Feigenbaum, K.V. Rajagopalan, Human sulfite oxidase R160Q: Identification of the mutation in a sulfite oxidase-deficient patient and expression and characterization of the mutant enzyme, Proceedings of the National Academy of Sciences of the United States of America, 95 (1998) 6394-6398.

[10] R. Hille, J. Hall, P. Basu, The mononuclear molybdenum enzymes, Chemical Reviews, 114 (2014) 3963-4038.

[11] Y. Wang, J. Mao, X. Meng, L. Yu, D. Deng, X. Bao, Catalysis with two-dimensional materials confining single atoms: Concept, design, and applications, Chemical Reviews, 119 (2019) 1806-1854.

[12] J. Deng, H. Li, J. Xiao, Y. Tu, D. Deng, H. Yang, H. Tian, J. Li, P. Ren, X. Bao, Triggering the electrocatalytic hydrogen evolution activity of the inert two-dimensional MoS_2 surface via single-atom metal doping, Energy & Environmental Science, 8 (2015) 1594-1601.

[13] Q. He, Y. Wan, H. Jiang, C. Wu, Z. Sun, S. Chen, Y. Zhou, H. Chen, D. Liu, Y.A. Haleem, B. Ge, X. Wu, L. Song, High-metallic-phase-concentration $Mo_{1-x}W_xS_2$

nanosheets with expanded interlayers as efficient electrocatalysts, Nano Research, 11 (2018) 1687-1698.

[14] Y. Shi, Y. Zhou, D.-R. Yang, W.-X. Xu, C. Wang, F.-B. Wang, J.-J. Xu, X.-H. Xia, H.-Y. Chen, Energy level engineering of MoS_2 by transition-metal doping for accelerating hydrogen evolution reaction, Journal of the American Chemical Society, 139 (2017) 15479-15485.

[15] Q. Zhang, L. Wang, J. Wang, X. Yu, J. Ge, H. Zhang, B. Lu, Semimetallic vanadium molybdenum sulfide for high-performance battery electrodes, Journal of Materials Chemistry A, 6 (2018) 9411-9419.

[16] X. Fan, Y. Zhou, G. Zhang, T. Liu, W. Dong, In situ photoelectrochemical activation of sulfite by MoS_2 photoanode for enhanced removal of ammonium nitrogen from wastewater, Applied Catalysis B: Environmental, 244 (2019) 396-406.

[17] H. Wang, C. Tsai, D. Kong, K. Chan, F. Abild-Pedersen, J.K. Nørskov, Y. Cui, Transition-metal doped edge sites in vertically aligned MoS_2 catalysts for enhanced hydrogen evolution, Nano Research, 8 (2015) 566-575.

[18] H. Li, L. Wang, Y. Dai, Z. Pu, Z. Lao, Y. Chen, M. Wang, X. Zheng, J. Zhu, W. Zhang, R. Si, C. Ma, J. Zeng, Synergetic interaction between neighbouring platinum monomers in CO_2 hydrogenation, Nature Nanotechnology, 13 (2018) 411-417.

[19] W. Xiao, P. Liu, J. Zhang, W. Song, Y.P. Feng, D. Gao, J. Ding, Dual-functional N dopants in edges and basal plane of MoS_2 nanosheets toward efficient and durable hydrogen evolution, Advanced Energy Materials, 7 (2017) 1602086.

[20] J. Miao, F.-X. Xiao, H.B. Yang, S.Y. Khoo, J. Chen, Z. Fan, Y.-Y. Hsu, H.M. Chen, H. Zhang, B. Liu, Hierarchical Ni-Mo-S nanosheets on carbon fiber cloth: A flexible

electrode for efficient hydrogen generation in neutral electrolyte, Science Advances, 1 (2015).

[21] J. Zhang, T. Wang, P. Liu, S. Liu, R. Dong, X. Zhuang, M. Chen, X. Feng, Engineering water dissociation sites in MoS_2 nanosheets for accelerated electrocatalytic hydrogen production, Energy & Environmental Science, (2016) 2789-2793.

[22] T. Chen, J. Ma, Q. Zhang, Z. Xie, Y. Zeng, R. Li, H. Liu, Y. Liu, W. Lv, G. Liu, Degradation of propranolol by UV-activated persulfate oxidation: Reaction kinetics, mechanisms, reactive sites, transformation pathways and Gaussian calculation, Science of the Total Environment, 690 (2019) 878-890.

[23] K. Chang, W. Chen, L-cysteine-assisted synthesis of layered MoS_2/graphene composites with excellent electrochemical performances for lithium ion batteries, ACS Nano, 5 (2011) 4720-4728.

[24] G. Kresse, J. Hafner, Ab initio molecular-dynamics simulation of the liquid-metal–amorphous-semiconductor transition in germanium, Physical Review B, 49 (1994) 14251.

[25] G. Kresse, J. Furthmüller, Efficient iterative schemes for ab initio total-energy calculations using a plane-wave basis set, Physical Review B, 54 (1996) 11169.

[26] P.E. Blöchl, Projector augmented-wave method, Physical Review B, 50 (1994) 17953.

[27] J.P. Perdew, K. Burke, M. Ernzerhof, Generalized gradient approximation made simple, Physical Review Letters, 77 (1996) 3865-3868.

[28] H.J. Monkhorst, J.D. Pack, Special points for Brillouin-zone integrations, Physical Review B, 13 (1976) 5188.

32

[29] S. Grimme, J. Antony, S. Ehrlich, H. Krieg, A consistent and accurate ab initio parametrization of density functional dispersion correction (DFT-D) for the 94 elements H-Pu, The Journal of Chemical Physics, 132 (2010) 154104.

[30] X.B. Min, Y.W.J. Li, Y. Ke, M.Q. Shi, L.Y. Chai, K. Xue, Fe-FeS$_2$ adsorbent prepared with iron powder and pyrite by facile ball milling and its application for arsenic removal, Water Science and Technology, 76 (2017) 192-200.

[31] J. Zolgharnein, M. Rastgordani, Multivariate optimization and characterization of simultaneous removal of binary mixture of Cu(II) and Pb(II) using Fe$_3$O$_4$@MoS$_2$ nanoparticles, Journal of Chemometrics, 32 (2018).

[32] G. Nagaraju, C.N. Tharamani, G.T. Chandrappa, J. Livage, Hydrothermal synthesis of amorphous MoS$_2$ nanofiber bundles via acidification of ammonium heptamolybdate tetrahydrate, Nanoscale Research Letters, 2 (2007) 461-468.

[33] S.V.P. Vattikuti, C. Byon, Synthesis and characterization of molybdenum disulfide nanoflowers and nanosheets: Nanotribology, Journal of Nanomaterials, (2015).

[34] P. Neta, R.E. Huie, One-electron redox reactions involving sulfite ions and aromatic amines, The Journal of Physical Chemistry, 89 (1985) 1783-1787.

[35] E. Hayon, A. Treinin, J. Wilf, Electronic spectra, photochemistry, and autoxidation mechanism of the sulfite-bisulfite-pyrosulfite systems. SO$_2^-$, SO$_3^-$, SO$_4^-$, and SO$_5^-$ radicals, Journal of the American Chemical Society, 94 (1972) 47-57.

[36] S. Reschke, D. Niks, H. Wilson, K.G. Sigfridsson, M. Haumann, K.V. Rajagopalan, R. Hille, S. Leimkuhler, Effect of exchange of the cysteine molybdenum ligand with selenocysteine on the structure and function of the active site in human sulfite oxidase, Biochemistry, 52 (2013) 8295-8303.

[37] G.N. George, C.A. Kipke, R.C. Prince, R.A. Sunde, J.H. Enemark, S.P. Cramer, Structure of the active site of sulfite oxidase. X-ray absorption spectroscopy of the Mo(IV), Mo(V), and Mo(VI) oxidation states, Biochemistry, 28 (1989) 5075-5080.

[38] M.C.F. Wander, K.M. Rosso, M.A.A. Schoonen, Structure and charge hopping dynamics in green rust, Journal of Physical Chemistry C, 111 (2007) 11414-11423.

[39] R. Codd, A.V. Astashkin, A. Pacheco, A.M. Raitsimring, J.H. Enemark, Pulsed ELDOR spectroscopy of the Mo(V)/Fe(III) state of sulfite oxidase prepared by one-electron reduction with Ti(III) citrate, Journal of Biological Inorganic Chemistry, 7 (2002) 338-350.

[40] S.O. Ganiyu, N. Oturan, S. Raffy, G. Esposito, E.D. van Hullebusch, M. Cretin, M.A. Oturan, Use of Sub-stoichiometric titanium oxide as a ceramic electrode in anodic oxidation and electro-Fenton degradation of the beta-blocker propranolol: Degradation kinetics and mineralization pathway, Electrochimica Acta, 242 (2017) 344-354.

[41] W. Tang, E. Sanville, G. Henkelman, A grid-based Bader analysis algorithm without lattice bias, Journal of Physics-Condensed Matter, 21 (2009).

[42] W. Zhang, P. Singh, D. Muir, Iron(II) oxidation by SO_2/O_2 in acidic media: Part I. Kinetics and mechanism, Hydrometallurgy, 55 (2000) 229-245.

[43] W. Zhang, P. Singh, D.M. Muir, SO_2/O_2 as an oxidant in hydrometallurgy, Minerals Engineering, 13 (2000) 1319-1328.
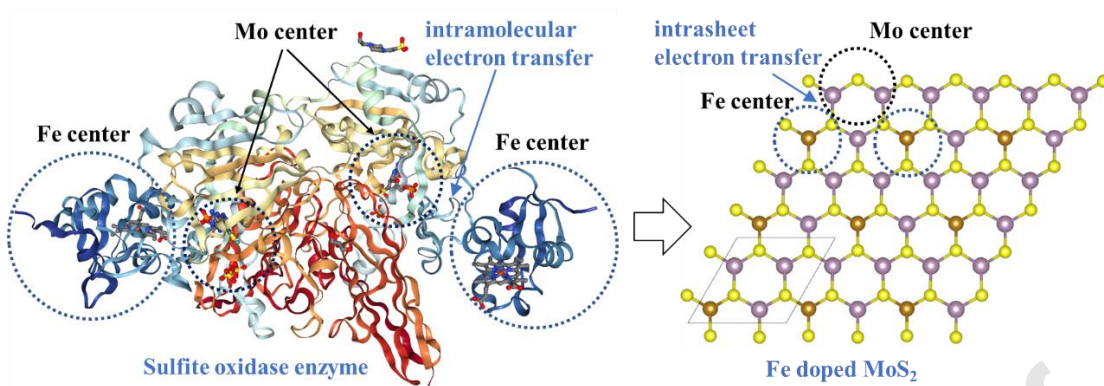
Figure 1. Schematic diagram of Fe doped MoS$_2$ mimicking sulfite oxidase enzyme.
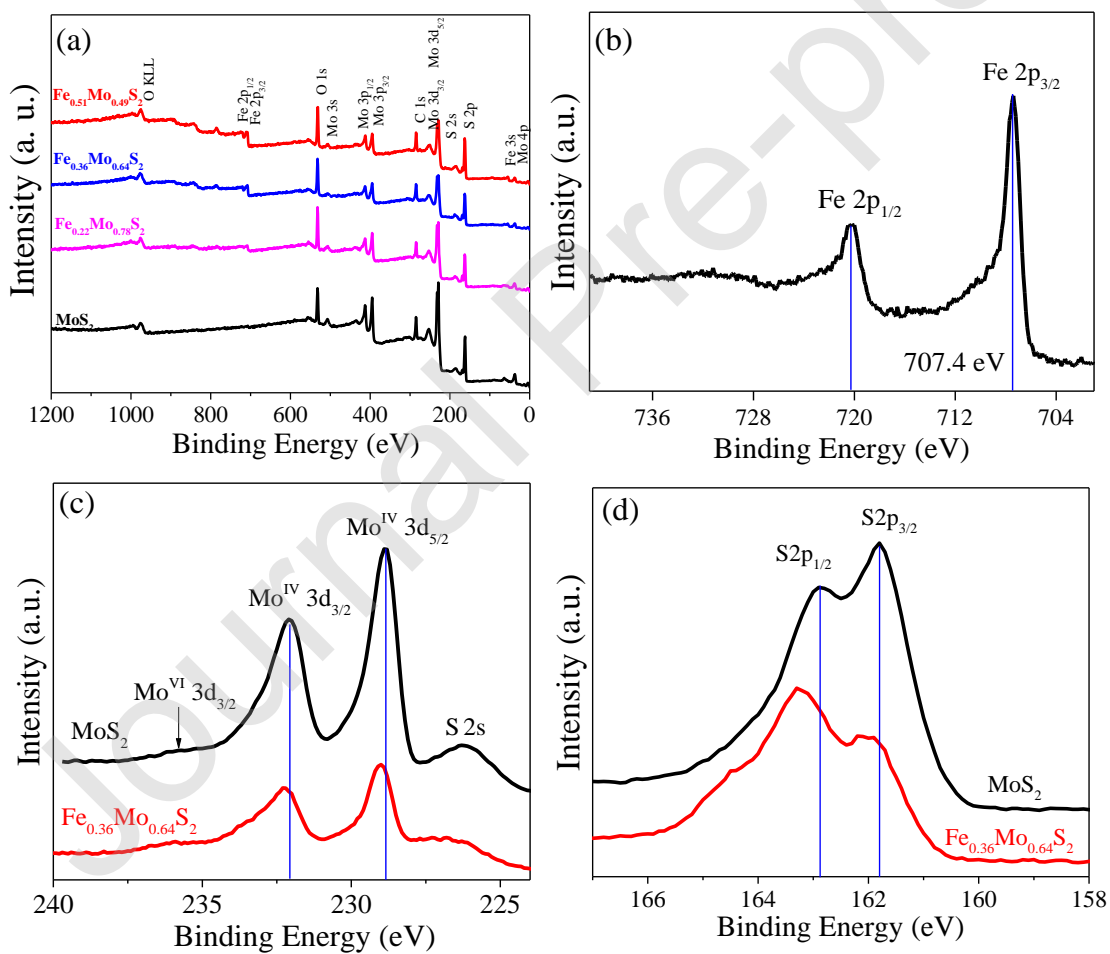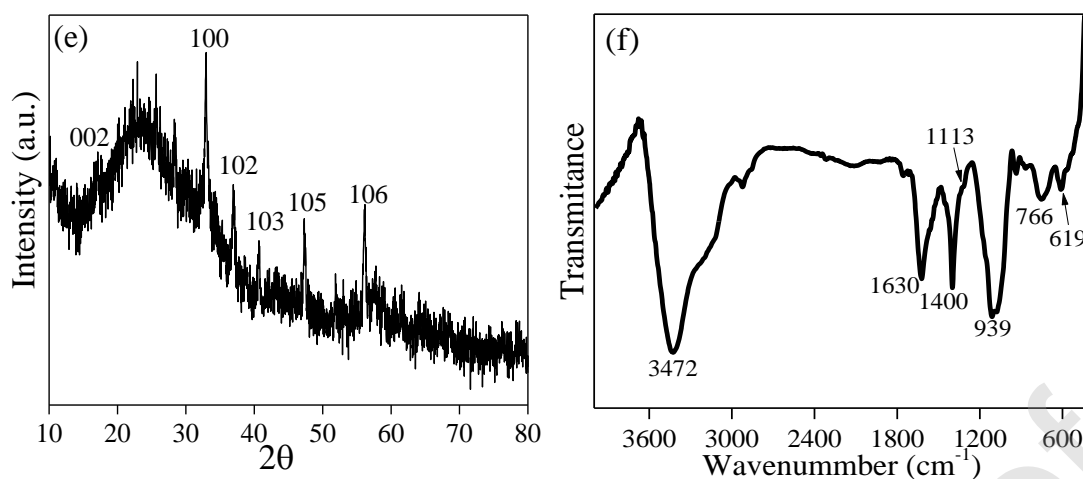
Figure 2. Spectral characterizations of Fe$_x$Mo$_{1-x}$S$_2$ catalysts. (a) XPS survey spectra of Fe$_x$Mo$_{1-x}$S$_2$ catalysts (x= 0, 0.22, 0.36 and 0.51). (b) Fe 2p, (c) Mo 3d, (d) S 2p high resolution XPS spectra, (e) XRD patterns and (f) FTIR spectrum of Fe$_{0.36}$Mo$_{0.64}$S$_2$ catalyst.

36
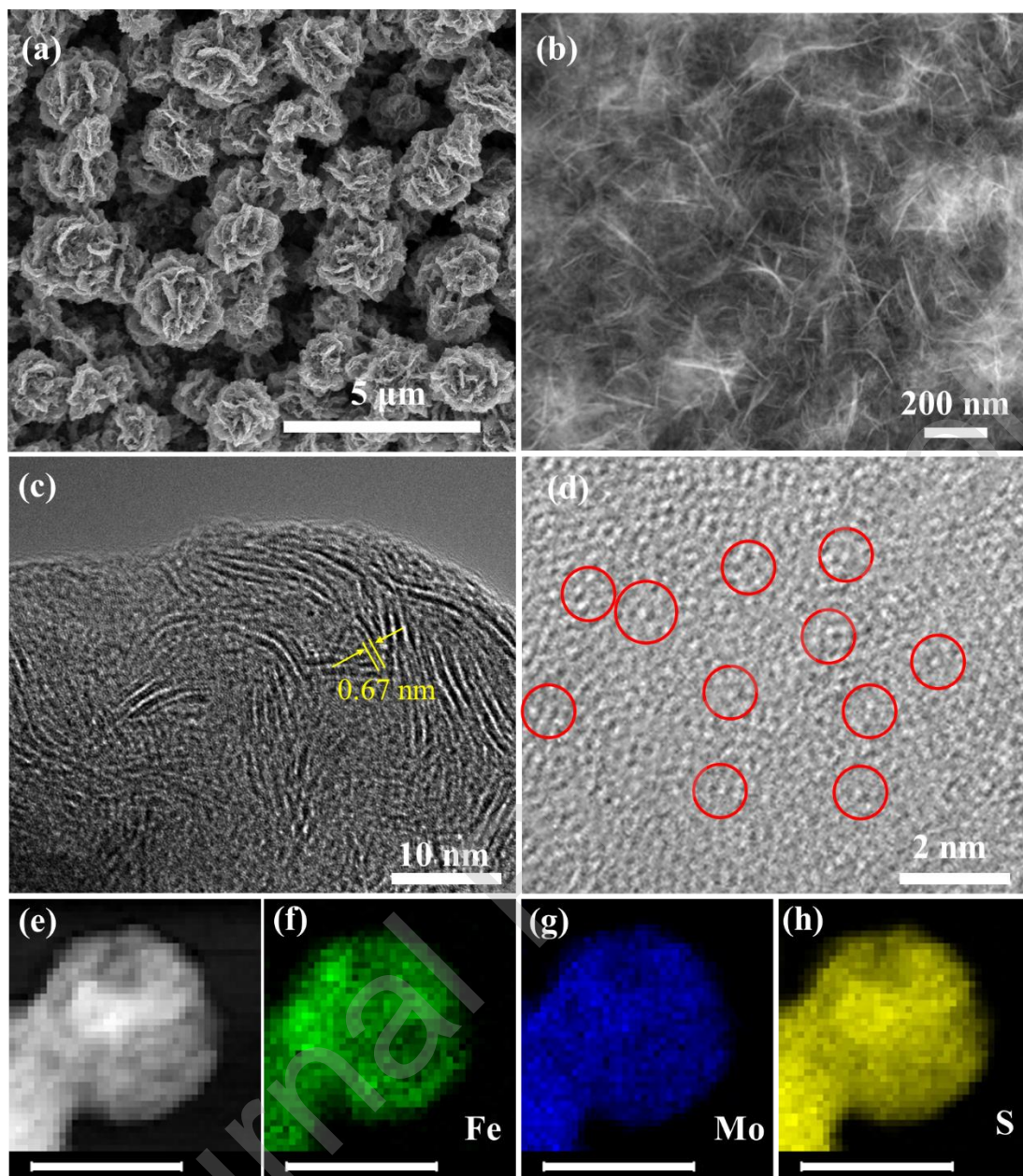
Figure 3. Microscopic characterizations of biomimetic $Fe_{0.36}Mo_{0.64}S_2$ catalyst. (a) SEM image, (b) STEM image, (c-d) HRTEM images, (e-h) the STEM image and the corresponding elemental mapping with scale bar = 50 nm.
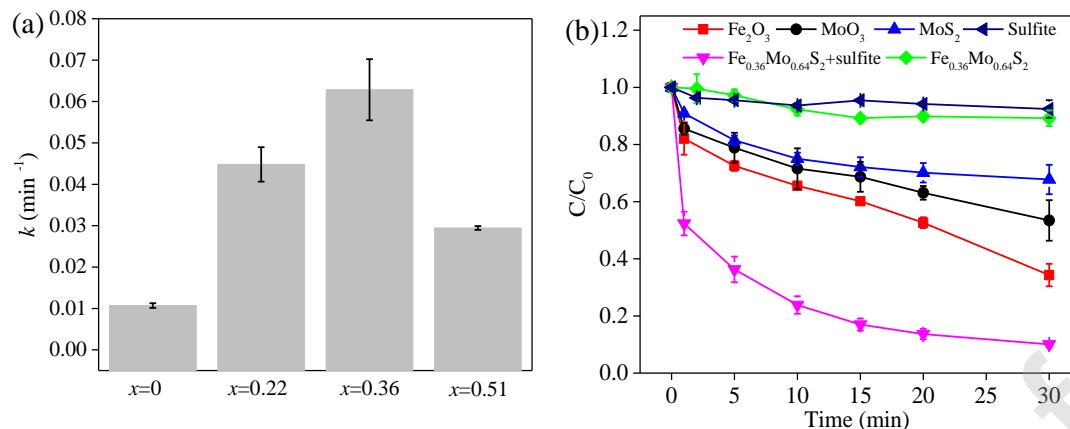
Figure 4. Catalytic performance of $Fe_xMo_{1-x}S_2$ for sulfite activation. (a) Effect of Fe content (x) in $Fe_xMo_{1-x}S_2$ on the reaction rate constant, $[Fe_xMo_{1-x}S_2]_0$=0.1 g/L, $[Na_2SO_3]_0$=1 mM, $[PPA]_0$=10 μM, pH=4.0. (b) PPA degradation in different systems, $[Fe_xMo_{1-x}S_2]_0$=$[Fe_2O_3]_0$=$[MoS_2]_0$=$[MoO_3]_0$=0.1 g/L, $[Na_2SO_3]_0$=1 mM, $[PPA]_0$=10 μM, pH=4.0.

38
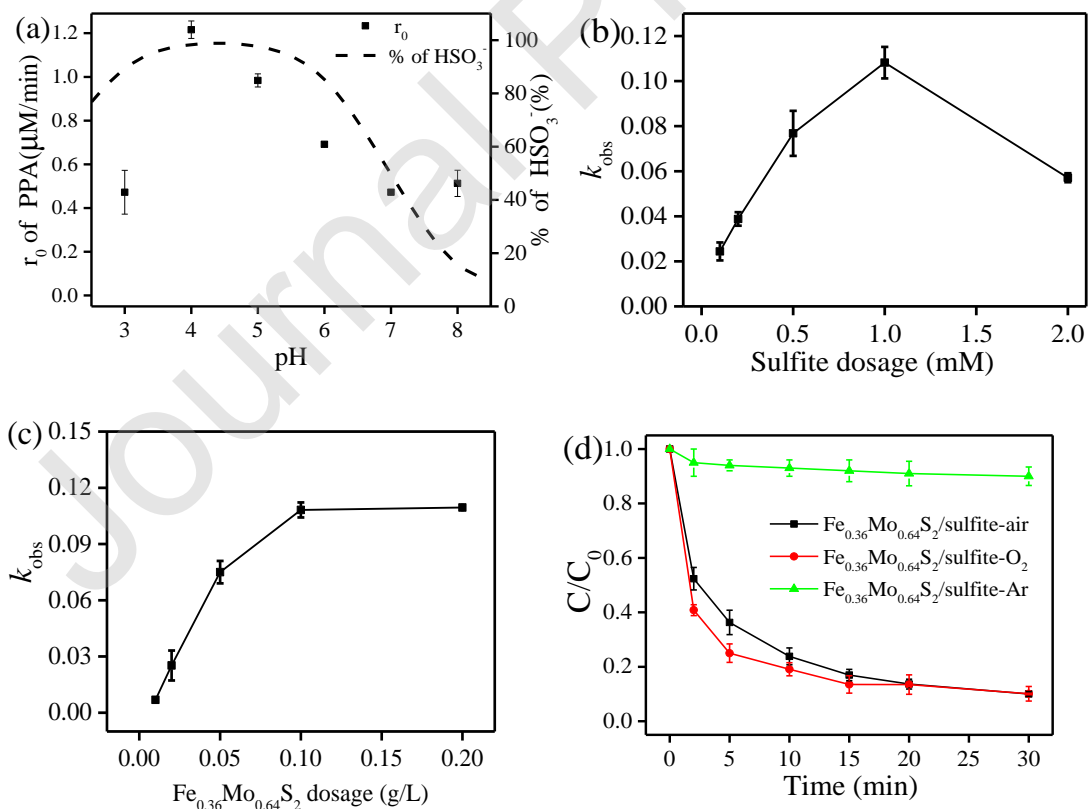
Figure 5. Effect of reaction parameters on the catalytic performance. (a) Effect of pH on initial reaction rate and the percentage of HSO_3^-, $[Fe_{0.36}Mo_{0.64}S_2]_0$=0.1g/L, $[Na_2SO_3]_0$=1 mM, $[PPA]_0$=10 μM. (b) Effect of sulfite concentration on apparent reaction rate constants, $[Fe_{0.36}Mo_{0.64}S_2]_0$= 0.1g/L, $[PPA]_0$=10 μM, pH=4.0. (c) Effect of $Fe_{0.36}Mo_{0.64}S_2$ dosage on apparent reaction rate constants, $[Na_2SO_3]_0$=1 mM, $[PPA]_0$=10μM, pH=4.0. (d) Effect of dissolved oxygen on PPA degradation in $Fe_{0.36}Mo_{0.64}S_2$/sulfite system. Experimental conditions: $[Fe_{0.36}Mo_{0.64}S_2]_0$=0.1 g/L, $[Na_2SO_3]_0$=1 mM, $[PPA]_0$=10 μM, pH=4.0
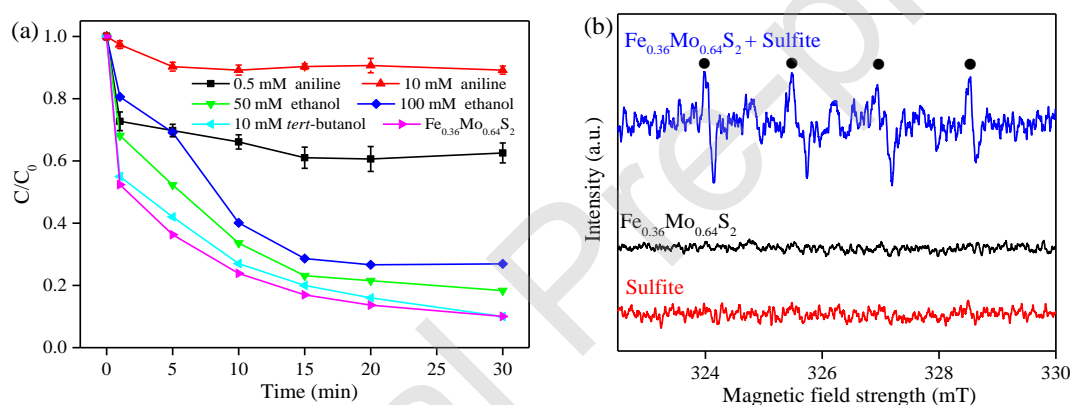
Figure 6. Identification of radicals in $Fe_{0.36}Mo_{0.64}S_2$/sulfite system. (a) Effect of radical scavengers (i.e. *tert*-butanol, ethanol, aniline) on PPA degradation. (b) ESR spectra of DMPO-$SO_3^{•-}$ radical adduct.
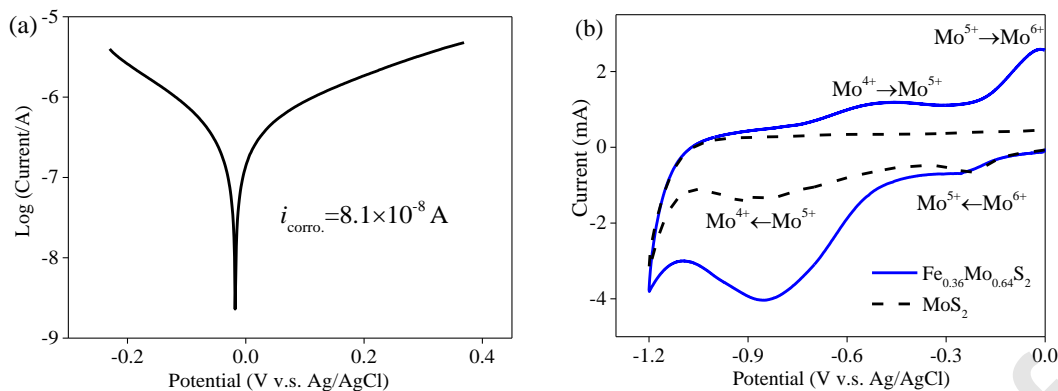
Figure 7. Identification of catalytic center in Fe$_{0.36}$Mo$_{0.64}$S$_2$/sulfite system. (a) Tafel scans of Fe$_{0.36}$Mo$_{0.64}$S$_2$ electrode in 1 mM Na$_2$SO$_3$ aqueous solution. (b) Cyclic voltammograms of Fe$_{0.36}$Mo$_{0.64}$S$_2$ and MoS$_2$, 0.5 M Na$_2$SO$_4$ O$_2$-free aqueous solution as supporting electrolyte.
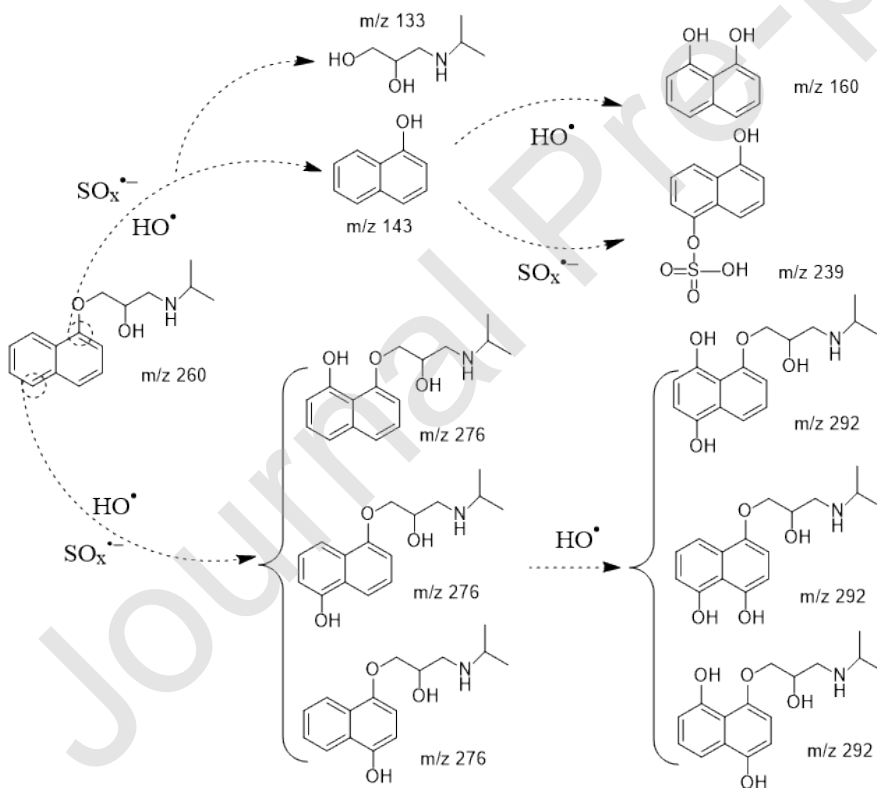
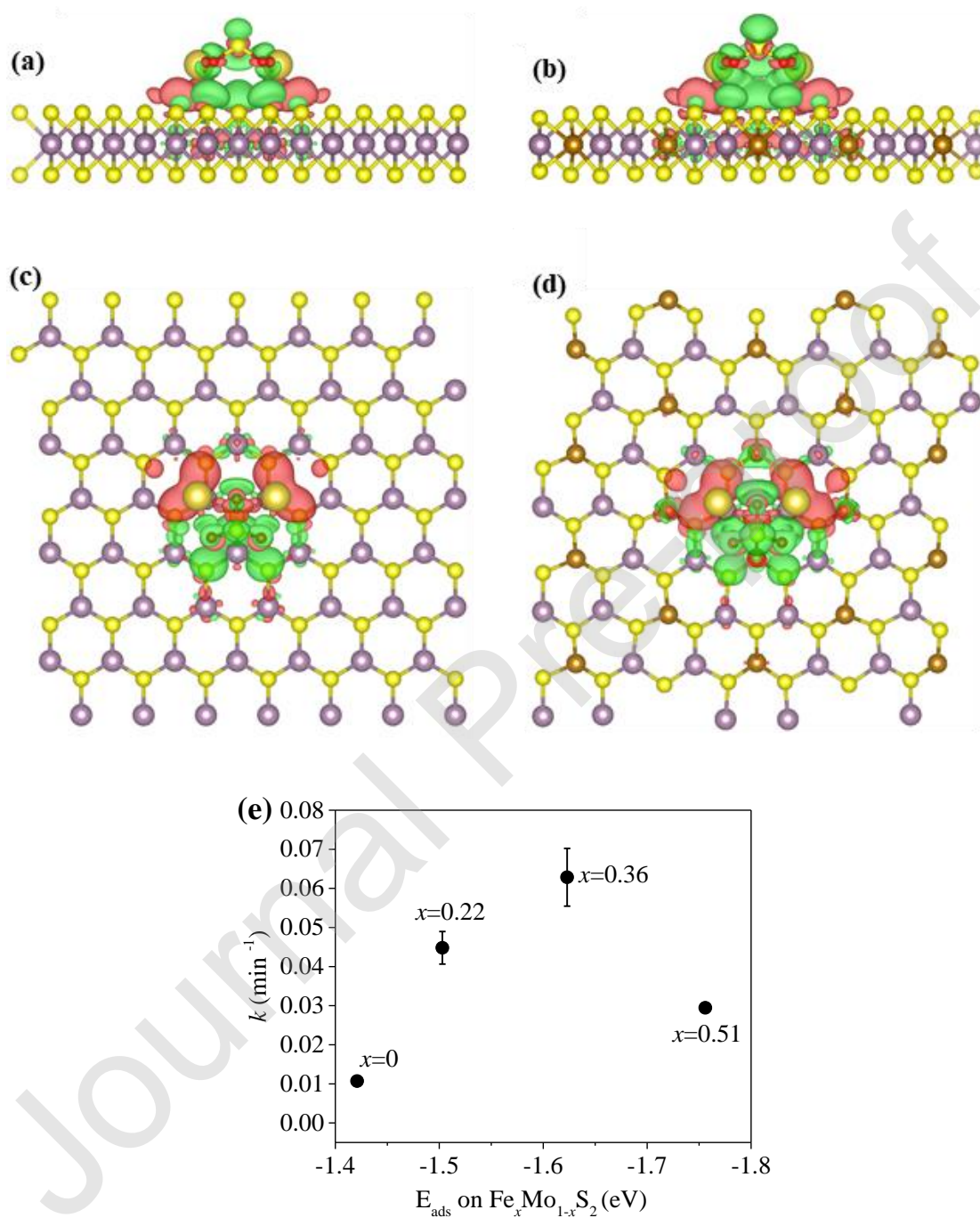Figure 8. Degradation path of PPA in Fe$_{0.36}$Mo$_{0.64}$S$_2$/sulfite system.

40

Figure 9. DFT calculations of Na_2SO_3 adsorption on catalyst. Top view and side view of the charge density difference for optimized configurations of Na_2SO_3 adsorbed on (a, c) MoS_2 and (b, d) $Fe_{0.36}Mo_{0.64}S_2$, respectively. Iso-surface contour is 0.001 $e/bohr^3$. The red

and green denote the electron accumulation and electron depletion, respectively. (e) Trends in reaction rate plotted as a function of the adsorption energy of sulfite on $Fe_{0.36}Mo_{0.64}S_2$.
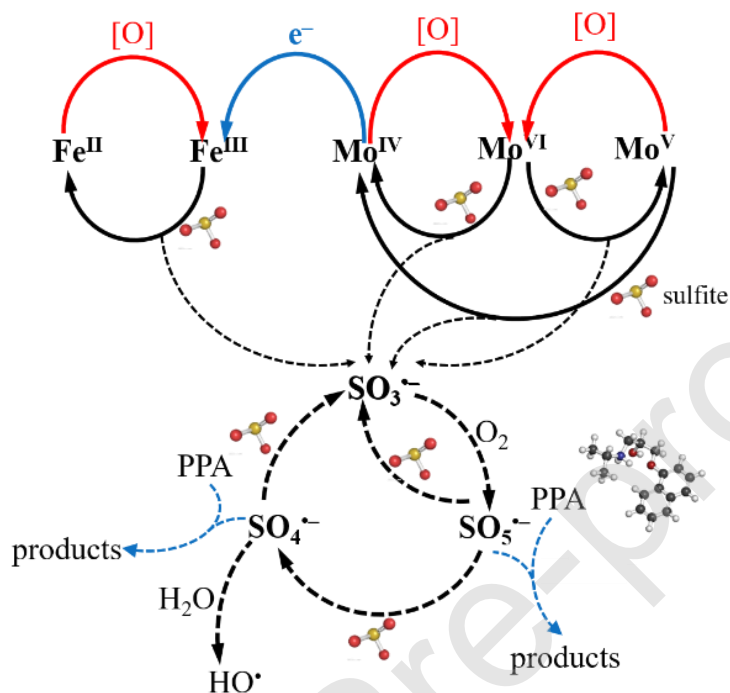

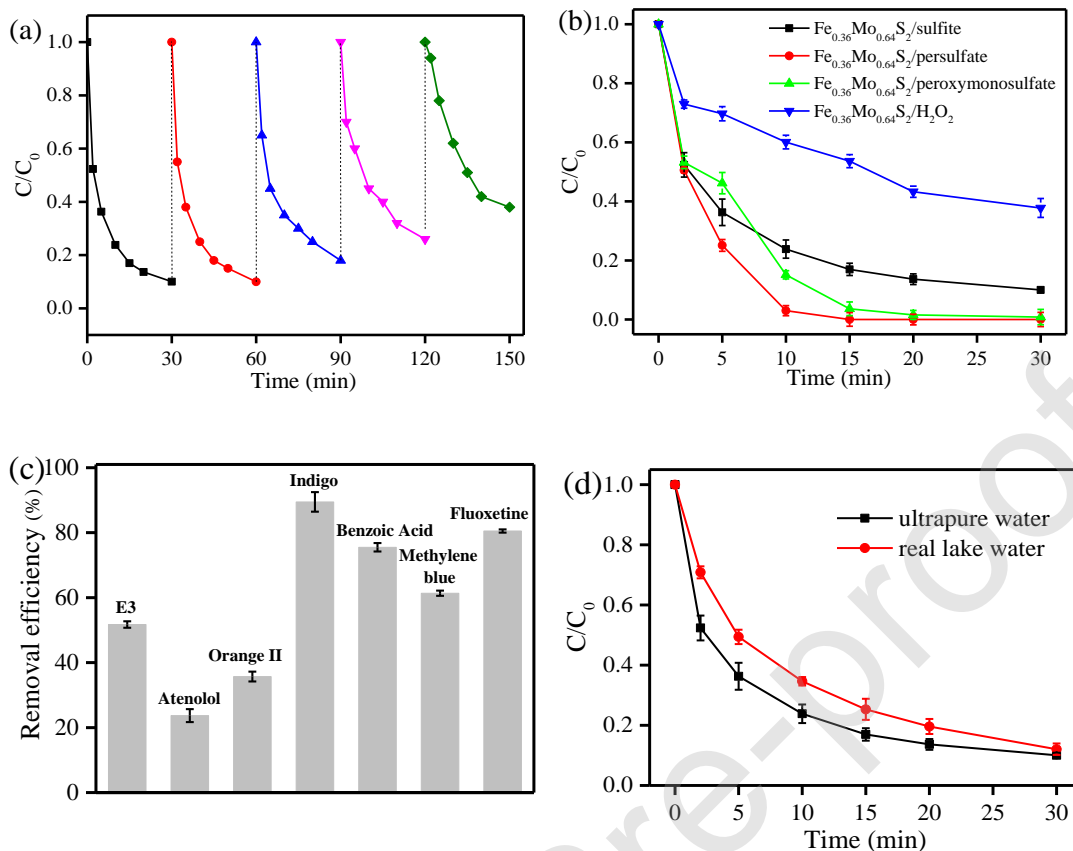Figure 10. The proposed overall sulfite activation mechanism on $Fe_xMo_{1-x}S_2$ catalyst.

Figure 11. Potential practical application of $Fe_{0.36}Mo_{0.64}S_2$ in advanced oxidation process. (a) reuse of $Fe_{0.36}Mo_{0.64}S_2$ catalyst in consecutive runs, $[Fe_{0.36}Mo_{0.64}S_2]_0$=0.1 g/L，$[Na_2SO_3]_0$=1 mM，$[PPA]_0$=10 μM，pH=4.0; (b) application of $Fe_{0.36}Mo_{0.64}S_2$ in other advanced oxidation systems. $[Fe_{0.36}Mo_{0.64}S_2]_0$=0.1g/L, $[Na_2SO_3]_0$=PS=PMS=H_2O_2=1mM，$[PPA]_0$=10μM，pH=4.0; (c) degradation of various organic pollutants in $Fe_{0.36}Mo_{0.64}S_2$/sulfite system, $[Fe_xMo_{1-x}S_2]_0$=0.1 g/L, $[Na_2SO_3]_0$=1 mM, [Organic pollutants]_0=10 μM, pH=4.0. (d) PPA removal by $Fe_{0.36}Mo_{0.64}S_2$/sulfite system in real lake water matrix, $[Fe_{0.36}Mo_{0.64}S_2]_0$=0.1 g/L, $[Na_2SO_3]_0$=1 mM, $[PPA]_0$=10 μM, pH=4.0.

43